# Stability investigations on the non-vdW-exfoliated surfaces of the topological insulator Bi_{2}Te_{3}: A first-principles study

Na Wang, Yiyang Sun, Yuyang Zhang, Damien West, Wenhui Duan, and Shengbai Zhang

# Stability investigations on the non-vdW-exfoliated surfaces of topological insulator Bi$_2$Te$_3$: a first-principles study

Na Wang[1], Yiyang Sun[2], Yuyang Zhang[2], Damien West[2],[*] Wenhui Duan[1,3], and Shengbai Zhang[2]

[1]*Department of Physics and State Key Laboratory of Low-Dimensional Quantum Physics,*
*Tsinghua University, Beijing 100084, People's Republic of China*
[2]*Department of Physics, Applied Physics, and Astronomy,*
*Rensselaer Polytechnic Institute, Troy, New York 12180, USA*
[3]*Collaborative Innovation Center of Quantum Matter, Tsinghua University, Beijing 100084, China*

(Dated: February 16, 2016)

The (0001) surface of Bi$_2$Te$_3$ is readily exposed by cleavage between two van der Waals (vdW) bonded quintuple layers (QLs) and it is widely accepted to be the most stable surface. However, little is known of the stability of other surfaces which may play important roles in growth, kinetics, and electronics. In this work, we identify the stability of the non-vdW-exfoliated surfaces of Bi$_2$Te$_3$ using first-principles density functional theory calculations. It is found that the energetics of the surfaces follows the order of (0001)→(01$\bar{1}$5)→(11$\bar{2}$0)→(01$\bar{1}$0)→(01$\bar{1}$ $\bar{1}$0)→(01$\bar{1}$4)-A/B→(01$\bar{1}$$\bar{1}$)-A/B→(02$\bar{2}$5), which can be understood almost entirely in terms of the density of dangling bonds on each surface. Using a modified Wulff construction theory, we determine an evolution diagram for sample geometry as a function of the binding of Bi$_2$Te$_3$ to the substrate. As binding to the substrate increases, the sample geometry transitions from 3-d to 2-d and from hexagonal to triangular in nature.

## I. INTRODUCTION

Topological insulators (TIs) are at the forefront of modern condensed matter physics[1–5]. The identification of pnictogen chalcogenides, such as bismuth telluride (Bi$_2$Te$_3$), as three dimensional TIs has sparked a tremendous amount of effort to prepare high-quality samples for investigation and to realize exotic technological applications. Molecular beam epitaxy (MBE) has been widely used to generate high quality TI films as it can be conducted under ultrahigh vacuum and can be highly controlled. MBE growth of Bi$_2$Te$_3$ is a van der Waals epitaxy process in the (0001)-orientation, proceeding quintuple layer(QL) by QL, so that large-scale (0001) surfaces on the top of the samples are naturally obtained[6–8]. In addition to MBE, chemical vapor deposition (CVD) is another important method to generate high-quality pnictogen chalcogenide materials with lower cost and greater flexibility. Even though the sample sizes are more limited, the samples also exhibit dominant (0001) surfaces[9,10].

The (0001) surface has been clearly established as the basal surface of pnictogen chalcogenides, however, very little is known about the other surfaces which must exist on finite samples. While topological band theory requires that each of the bounding surfaces for an isolated TI sample have a topologically protected state, the details of the spin-texture and the location of the Dirac point relative to the band edges can be substantially different on different surfaces[11,12]. As TIs become more mature, knowledge of these terminal surfaces and their effects on the spin-current, for instance, will become an increasingly important factor for device design. While the shapes of as-grown samples can often be understood by the symmetry of the system[13–15], the commonly ob-served flake-like shapes in MBE-grown Bi$_2$Te$_3$ samples and the nano-structures in CVD-grown Bi$_2$Te$_3$ samples differ based on growth conditions, being either triangular or hexagonal, both of which satisfy the C$_{3v}$ symmetry of Bi$_2$Te$_3$[16,17]. This indicates that under the experimentally realizable growth conditions, various differences in the surface stability may play an important role in determining not only the shape of the sample, but also the topological properties of the non-basal surfaces.

In this work, we systematically investigate the energetics of the surfaces of Bi$_2$Te$_3$ using first-principles density functional theory (DFT) calculation. We show that the stability of the surfaces follows the ordering of (0001)→(01$\bar{1}$5)→(11$\bar{2}$0)→(01$\bar{1}$0)→(01$\bar{1}$ $\bar{1}$0) →(01$\bar{1}$4)-A/B→(01$\bar{1}$$\bar{1}$)-A/B→(02$\bar{2}$5), note that for readability we will use the Roman numeral X to represent $\bar{1}$0 in the following. This energy ordering can be understood almost entirely in terms of the density of dangling bonds on each surface. Due to the particularly low energy of the (01$\bar{1}$5) surface (approximately 0.18 J/m$^2$ larger than (0001)), the sidewalls of as-grown samples are predicted to be (01$\bar{1}$5) surfaces, instead of being perpendicular to the basal (0001) surface. Using a modified Wulff construction theory, we determine an evolution diagram of the sample geometries which minimize the total system energy as a function of the binding of Bi$_2$Te$_3$ with substrate.

## II. METHODS

Our DFT calculations were performed with the Vienna Ab initio Simulation Package (VASP).[18] The interaction between ion cores and valence electrons was described by the projector augmented wave (PAW) method.[19] We
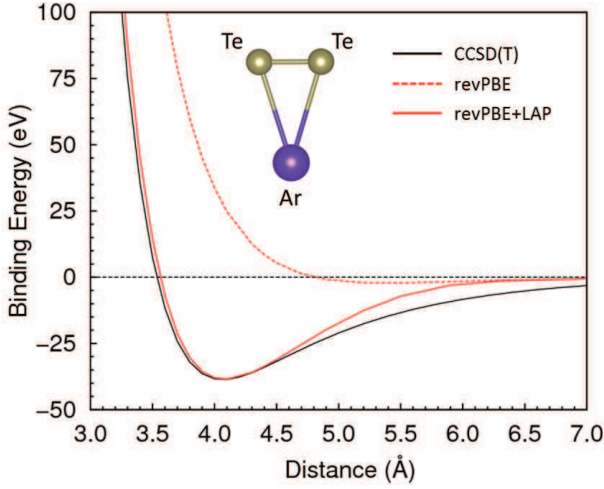
FIG. 1: (Color online) Determination of the LAP correction parameter using the interaction energy curve between a Te dimer and an Ar atom obtained by coupled-cluster method with single, double, and perturbative triple excitations (or CCSD(T) method)[20] used as a benchmark. The parameters for this curve is $c_0 = 62$ Ry Bohr, $n = 6$, $v_{const} = 6.5 \ 10^{-4}$ Ry.

used a plane wave basis set with a kinetic energy cutoff of 272 eV. Integration of Brillouin zone was performed with sufficient k-point sampling[21]: $9 \times 1 \times 1$, $5 \times 4 \times 1$, $9 \times 3 \times 1$, $2 \times 2 \times 1$ and $4 \times 4 \times 1$ for $(01\bar{1}0)$, $(11\bar{2}0)$, $(01\bar{1}\ \bar{1}0)$, $(02\bar{2}5)$ and $(01\bar{1}4)/(01\bar{1}\bar{1})/(01\bar{1}5)$ surfaces, respectively. The surfaces were modeled by atomic slabs separated by vacuum regions of approximately 10Å. The surfaces were modeled in supercells containing 13, 21, 26 and 27 atomic layers for the $(11\bar{2}0)/(01\bar{1}5)/(01\bar{1}\ \bar{1}0)$, $(01\bar{1}0)$, $(01\bar{1}4)/(01\bar{1}\bar{1})$ and $(02\bar{2}5)$ surfaces, respectively. The thickness of the slabs were chosen such that increasing the slab thickness led to a change in the calculated surface energy of less than 0.001 J/m$^2$. The supercell used for the calculation of each surface is shown by the solid lines in Fig. 4. All atoms were fully relaxed until the forces on atoms were smaller than 0.025 eV/Å.

As the generalized gradient approximation (GGA)[22] consistently underestimates the strength of vdW interaction, the primary functional used in these calculations is based on the local density approximation(LDA)[23]. However, GGA calculations for surface energies are also conducted as in Fig. 3 (c) in order for comparison. Additionally, calculations of the three low energy surfaces (found within the LDA) were also performed using the revised Perdew-Burke-Ernzerhof (revPBE) functional[24] which was modified by adding an attractive local atomic potential (LAP)[25] in order to more accurately reproduce vdW interaction in this system. The procedure described in Ref. 25 is used to determine the LAP parameters and the interaction energy curve between a Te dimer and an Ar atom obtained by coupled-cluster method with single, double, and perturbative triple excitations (or CCSD(T) method)[20] was used as a benchmark, as is shown in Fig.

TABLE I: Lattice parameters of $Bi_2Te_3$ crystal. a and c are measured in Å, while u and v are dimensionless internal parameters. The experimental results are taken from Ref. 26.

|           | a             | c              | u     | v     |
|-----------|---------------|----------------|-------|-------|
| LDA       | 4.354 (-0.7%) | 29.87 (-2.1%)  | 0.400 | 0.209 |
| LDA+SO    | 4.369 (-0.4%) | 29.60 (-3.0%)  | 0.401 | 0.207 |
| PBE       | 4.460 (1.7%)  | 31.52 (3.3%)   | 0.398 | 0.214 |
| revPBE+LAP| 4.441 (1.3%)  | 31.15 (2.1%)   | 0.399 | 0.212 |
| Exp.      | 4.386         | 30.50          | 0.400 | 0.210 |

1. It can be seen that after adding the LAPs, the equilibrium binding distance and binding energy can both be well reproduced in DFT calculations. The fitted LAP parameters for Te ($c_0 = 62$ Ry Bohr, $n = 6$, $v_{const} = 6.5 \ 10^{-4}$ Ry) were directly applied to the calculations in $Bi_2Te_3$ calculations.

Table I lists the calculated lattice parameters of $Bi_2Te_3$ from these methods compared with experiment.[26] While all methods yield reasonable agreement with the experimental results, the internal parameters u and v and the lateral lattice constants, a, are better described than the lattice constant associated with the vdW interaction, c. As is typical in vdW systems, LDA tends to overbind yielding a slightly underestimated ($\approx 2\%$) c and revPBE+LAP still tends to underbind, yielding c elongated by $\approx 2\%$. PBE further overestimates c by 3.3%. As spin-orbit interaction has been shown to qualitatively effect the energy ordering of defects in this system[27], LDA calculations including spin-orbit interaction implemented in the all-electron part of the PAW Hamiltonian were conducted for each of the $Bi_2Te_3$ surfaces considered in this work.

## III. RESULTS AND DISCUSSION

The crystal structure of $Bi_2Te_3$ is rhombohedral with the space group $D_{3d}^5$ (R$\bar{3}$m)[16], and as shown in Fig. 2. The crystal is layered in the z-direction with strong bonding within the quintuple layers (QLs), consisting of Te1-Bi-Te2-Bi-Te1, and weak van der Waals bonding between QLs. Note that the bonding is primarily octohedral and could be viewed as existing in a rock salt structure (distorted along [111]) with a recurring missing layer of cations between the QLs. We take this view in order to systematically identify potential low energy surfaces analogous to the low-energy surfaces (001), (110), and (111) which are typically associated with rock salt structures.[28–31] Hence, we calculate the surfaces of $Bi_2Te_3$ which directly corresponded to the low-index surfaces of the rock salt structure, e.g. , $(01\bar{1}5)$ to (001), $(01\bar{1}X)$ to (110), and also (0001) and $(02\bar{2}5)$, both of which corresponded to the (111) surface of the rock salt structure.

In the rock salt structure, the (111) surfaces along different directions are identical, however, in $Bi_2Te_3$, the (0001) and $(02\bar{2}5)$ surfaces both correspond to the (111)
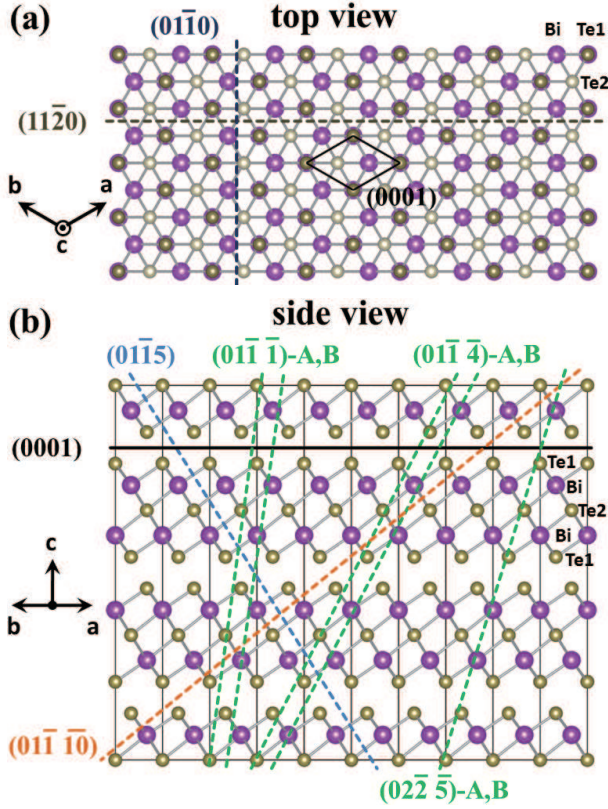
FIG. 2: (Color online) (a) Top and (b) side view of 3 QL $Bi_2Te_3$. Other than the basal (0001) surface, the other two low-index surfaces, namely (11$\bar{2}$0) and (01$\bar{1}$0), are both perpendicular to the (0001) surface. In addition, the side view in Fig. 2(b) clearly shows other possible cuts of the crystal, which result in surfaces that are inclined from the [0001] direction, namely (011$\bar{5}$), (01$\bar{1}$ $\bar{1}$0) and (02$\bar{2}$ $\bar{5}$) non-polar surfaces and (01$\bar{1}$4)-A/B and (01$\bar{1}\bar{1}$)-A/B polar surfaces.

surface of rock salt, but are distinct due to distortion and the missing cation layer in $Bi_2Te_3$. In addition to the missing cation layer, there is a relative slip between the two QLs, from which we find another two additional types of polar surfaces (01$\bar{1}\bar{4}$)-A/B and (01$\bar{1}\bar{1}$)-A/B, which are similar to the (111) polar surfaces of the rock salt structure. In addition to these surfaces, we have also calculated the low-index surfaces of $Bi_2Te_3$ which are perpendicular to the basal (0001). The orientations of each of these considered surfaces can be seen from the cutting planes shown in Fig. 2(b) and the structure and chemistry of the surface termination can be seen in Fig. 4. Note that while atomic relaxation of these cut surfaces allows for some reconstruction, we do not consider reconstructions of the surface which include vacancies or adatoms.

The surface energy, $\sigma$, is calculated according to[32–36]

$$\sigma = [E_{\text{slab}}(N) - E_{\text{bulk}}(N) - \sum n_i\mu_i]/2A, \qquad (1)$$

where $E_{\text{slab}}(N)$ and $E_{\text{bulk}}(N)$ are the total energy of $N$ formula units of $Bi_2Te_3$ in a slab and bulk environment,
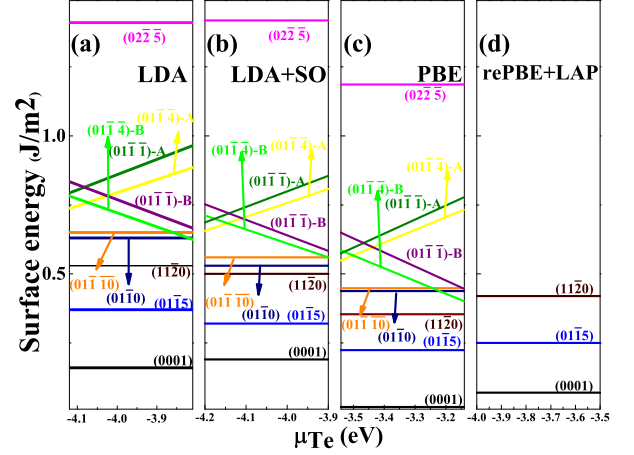


FIG. 3: (Color online) Calculated surface energies as a function of the chemical potential of Te $\mu_{\text{Te}}$ using (a) LDA, (b) LDA with SOC interactions, (c) PBE and (d) revPBE with LAP corrections as xc functionals, respectively.

respectively, and $2A$ is the total exposed surface area (corresponding to the two identical surfaces present in the supercell calculation) of the slab. $n_i$ indicates the number of atoms of type $i$ that have been added to ($n_i > 0$) or removed from ($n_i < 0$) the supercell when the surface is created, and $\mu_i$ are the corresponding chemical potentials of these species. Under the Bi (Te) rich growth conditions, the chemical potential of Bi (Te) is determined from its bulk phase, while the chemical potential of Te (Bi) is determined such that $2\mu_{\text{Bi}}+3\mu_{\text{Te}} = \mu_{\text{Bi}_2\text{Te}_3}$, where $\mu_{\text{Bi}_2\text{Te}_3}$ is the energy per formula unit of bulk $Bi_2Te_3$. In our calculations, the hexagonal scalenohedral phase of Bi as well as trigonal-trapezohedral phase of Te[37] were used as the reference elemental bulk phases for the chemical potentials.

We first turn our attention to the basal (0001) surface, which is the dominant surface of as-grown samples and is readily exposed by cleaving between two QLs. As shown in Fig. 3, all four methods yield the result that the surface energy of the (0001) surface is significantly smaller than other surfaces, consistent with the fact that only vdW bonds are broken in its formation. Calculation also shows that the surface energy is well converged (within 0.01 J/m$^2$) even for a single QL and that there is nearly no appreciable atomic relaxation relative to a bulk terminated surface. According to LDA calculation, the relaxation energy is less than 2.6 meV per surface unit cell. Notably, the calculated (0001) surface energy using the PBE functional almost entirely vanishes, highlighting the importance of accounting for vdW interactions. Better representing the vdW interaction through the LAP correction increases this surface energy to 0.07 J/m$^2$.
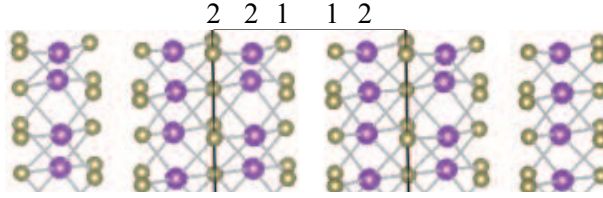
The energy ordering of the non-basal surfaces were found to be quite insensitive to the functional used or the inclusion of spin-orbit interaction, as seen in Fig. 3. While the surface energies obtained from revPBE+LAP
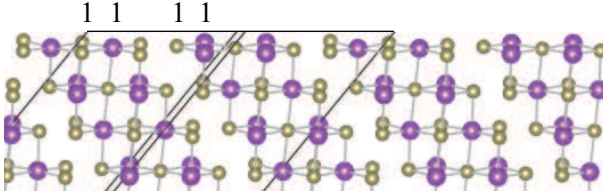
**_Non-polar surfaces:_**
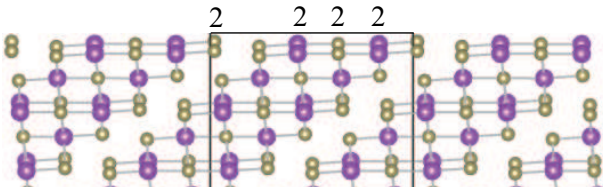
**(a)** $(01\bar{1}0) : (100) : (111)$      $\sim 0.12$
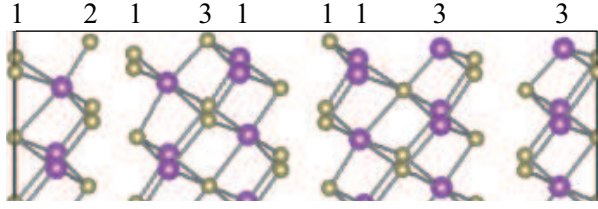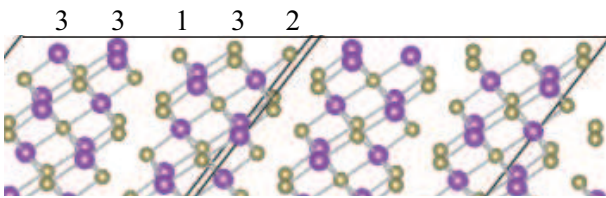
**_Polar surfaces:_**

**(f)** $(01\bar{1}\bar{4})$-A $: (01\bar{4})$-A $: (211)$-A     $\sim 0.12$

**(b)** $(11\bar{2}0) : (221) : (110)$      $\sim 0.10$

**(g)** $(01\bar{1}\bar{4})$-B $: (01\bar{4})$-B $: (211)$-B     $\sim 0.12$

**(c)** $(01\bar{1}5) : (015) : (221)$      $\sim 0.08$
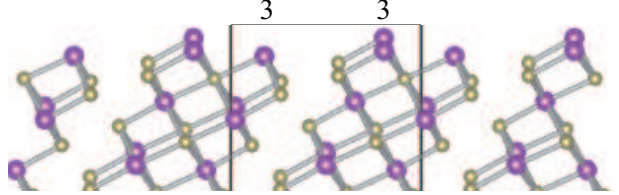
**(h)** $(01\bar{1}\bar{1})$-A $: (01\bar{1})$-A $: (100)$-A     $\sim 0.14$

**(d)** $(01\bar{1}\ \bar{1}0) : (01\ \bar{1}0) : (334)$      $\sim 0.11$
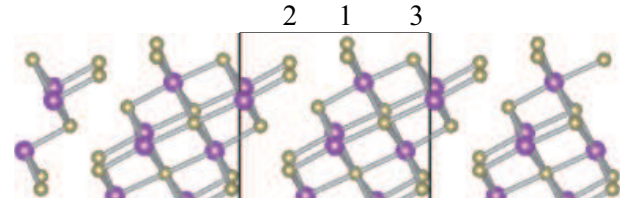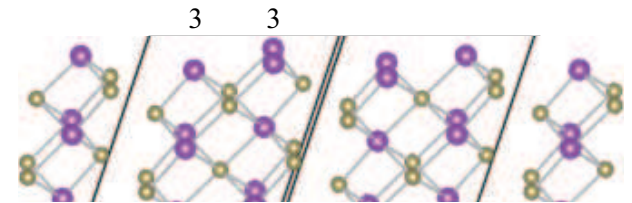
**(i)** $(01\bar{1}\bar{1})$-B $: (01\bar{1})$-B $: (100)$-B     $\sim 0.14$

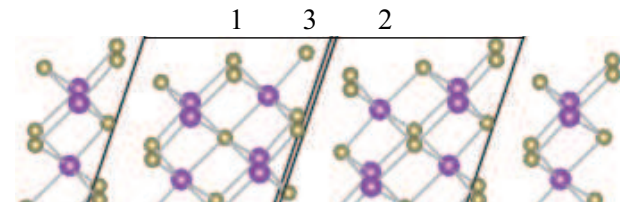**(e)** $(02\bar{2}5) : (025) : (113)$      $\sim 0.13$



FIG. 4: (Color online) Relaxed structures of non-basal terminating surfaces. The orientation of each surface is labeled by three different sets of indices separated by colons, corresponding to Miller-Bravais, hexagonal and rhombohedral, respectively. The supercell used for the calculation of each surface is shown by the solid lines. The number above each of the topmost atoms at each surface indicate the numbers of bonds broken for that atom in the creation of the surface. The average number of broken bonds per unit surface area ($\text{Å}^2$), for each surface, is indicated by the number to the right of the indices.

tend to be slightly lower than those calculated from LDA, the overbinding in the LDA appears to be a somewhat systematic error which yields a rigid shift in the calculated surface energies, not effecting the ordering of the three lowest energy surfaces. The effect of the SOI is also visible when comparing Fig. 3 (a) and (b). Here it can be seen that SOI leaves the surface energy ordering unchanged over nearly the entire range of chemical potential. The largest effect associated with SOI seems to be the tendency to preferentially stabilize the non-basal surfaces, relative to (0001), which may be understood due to the presence of Bi dangling bonds on these surfaces and the large atomic SOI associated with Bi.

The lowest energy non-basal surface was found to be the high-index $(01\bar{1}5)$ surface, regardless of method or $\mu_{Te}$. Considering that creating the (0001) surface requires only to overcome vdW binding, the finding that $(01\bar{1}5)$ is only twice as energetic as (0001), within LDA, is quite surprising (approximately 3.5 times as energetic within revPBE+LAP). To understand this, we examine the chemical nature of the surface termination of $(01\bar{1}5)$, as shown in Fig. 4(c). While in bulk each atom has six nearest neighbors (nn's) (Bi and Te2 form covalent/ionic bonds with all six nn's, while Te1 form three covalent/ionic bonds with Bi and vdW bonds with Te in the nearby QL), here on the topmost layer of a $(01\bar{1}5)$ surface, all atoms have only one less nn compared with that in bulk. On average, this yields only 0.8 dangling bonds per atom on the surface, and subsequently it has a significantly lower surface energy than any of the other non-basal surfaces. As mentioned previously, the $(01\bar{1}5)$ surface is analogous to the (001) surface of the rock salt structure, and the low energy of the $(01\bar{1}5)$ surface in $Bi_2Te_3$ is consistent with the fact that the (001) surface tends to be the lowest-energy surface in the rock salt structure.

In considering the number of dangling bonds per unit area at the surface, as given in Fig. 4, we find that this almost entirely explains the observed ordering in surface stability. The primary exception being the $(01\bar{1}0)$ surface, which from counting dangling bonds we would expect to be very slightly higher in energy than the $(11\bar{2}0)$ surface, but from Fig. 1, we see the opposite is true. This exception can be understood due to the large surface roughness of $(01\bar{1}0)$ which allows for more stabilization through the structural relaxation of Te at the surface. As the surface energies of the polar surfaces $(01\bar{1}4)$-A/B and $(01\bar{1}\bar{1})$-A/B are stoichiometrically different than bulk, they are explicit linear functions of the chemical potential of Te, with the Te(Bi)-terminated surface more favored under Te(Bi)-rich conditions. As can be seen from their top view in Fig. 4, while the chemical bonding of the $(01\bar{1}4)$ and the $(01\bar{1}\bar{1})$ surfaces are similar, the exposed area of $(01\bar{1}\bar{1})$ is smaller than $(01\bar{1}4)$, leading to a surface energy of $(01\bar{1}\bar{1})$ which is generally higher than the $(01\bar{1}4)$ surface. The exact (111)-corresponded surface $(02\bar{2}\bar{5})$ possesses somewhat unexpectedly high energy, this suggests that there may be charge polarization
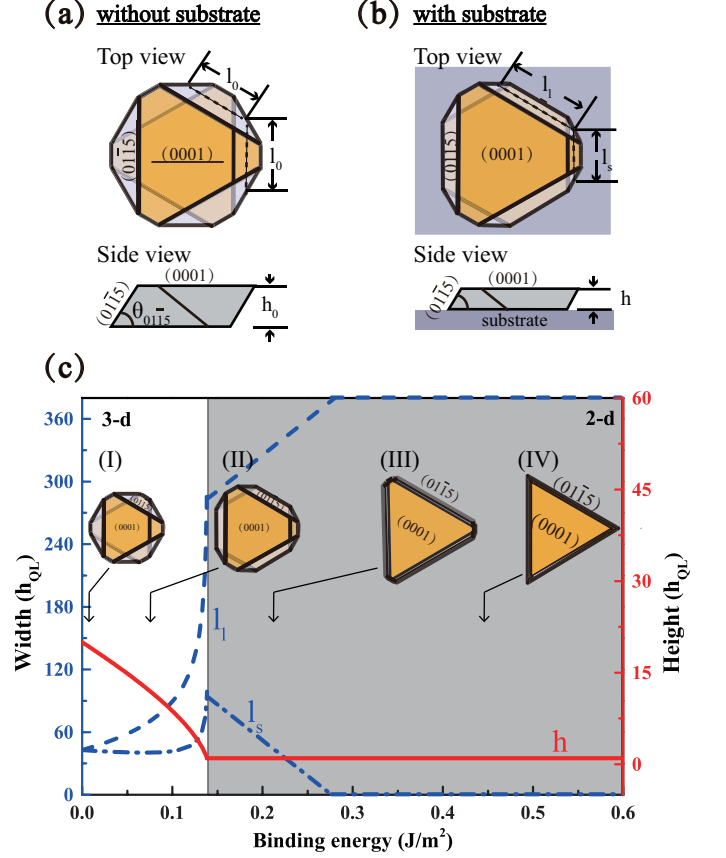


FIG. 5: (Color online) The top and side view of the $Bi_2Te_3$ crystal constructed by using the Wulff construction theory and the surface energies calculated with the PBE+LAP method (a) without substrate and (b) with substrate. The lateral size and the thickness for the nanoplate without substrate are labeled as $l_0$ and $h_0$, and those for the nanoplate with substrate are labeled as $l_{l/s}$ and h. The basal and lateral surfaces are (0001) and $(01\bar{1}5)$, respectively, and the angle between the lateral and basal surface is labeled as $\theta_{01\bar{1}5}$. (c) The size evolution of the nanoplate with constant volume under thermo-equilibrium condition as the function of the binding energy with substrate, with the left and right axis for the lateral $l_{l/s}$ and vertical size $h$, respectively. The shapes at four typical positions of the binding energy are also shown in the figure pointed by the arrows.

within the surface due to the alternating Te and Bi termination for adjacent QLs, as can be seen in Fig. 4(e).

Based on the calculated surface energies, the overall shape of the 3-d thermo-equilibrium crystal in vacuum can be constructed following the 3-d Wulff construction theory[38] - wherein the distances of the crystal faces from a point within the crystal (called a Wulff's point) are proportional to the corresponding specific surface energies of these faces. This lowest energy crystal shape is shown in Fig. 5(a) and appears hexagonal in shape with (0001) as the basal surfaces and $(01\bar{1}5)$ as the lateral surfaces which form an angle of 58° with the basal surfaces. The ratio between the lateral size (characterized by

the side length of the cross-section at the median height of the nanoplate) $l_0$ and the vertical thickness $h_0$ is approximately 2.1 within the PBE+LAP method (or 1.4 within LDA surface energies), both of which are relatively small compared with experiment[39–41]. However, we note that binding with the substrate can modify the equilibrium shape of the crystal[38,42], which may explain the various shapes observed for nanoplate growth on substrate in experiment[6–10]. For the case of binding to the substrate, the top and bottom surface energies become inequivalent– leading to a reduction in the symmetry of the Wulff construction, as shown in the schematic Fig. 5(b). As the area of the surface bound to the substrate becomes larger relative to the top basal surface, the shape is now characterized by two inequivalent lateral dimensions labeled $l_{l(ong)}$ and $l_{s(hort)}$, in addition to $h_0$.

The evolution of the dimensions of the energy minimizing shapes, for surface energies calculated with revPBE+LAP, with increasing binding to the substrate is shown in Fig. 5 (c), where we consider a sample of constant volume $V_0$ (corresponding to a nanoplate of 20 QLs height that satisfies the Wulff construction shown in Fig. 5(a)). For weak binding, the 3-d Wulff construction theory is straightforwardly modified by considering the energy of the bottom surface to be lowered by the binding energy. Here it can be seen that as the binding increases, the sample becomes flatter and more triangular as shown in inset (II), with $h$ decreasing and $l_l/l_s$ increasing. Note that in actuality, the continuous curve representing $h$ in Fig. 5(c) should be quantized to integer numbers of quintuple layers due to strong intralayer binding which is neglected in the Wulff construction which assumes a continuous bulk medium. Furthermore, as the binding becomes sufficiently large with $h$ becoming 1QL, the 3-d Wulff construction completely breaks down. Due to the discrete nature of the quintuple layers, as $h$ becomes 1QL we transition from 3-d to 2-d growth and $h$ can be diminished no further.

This transition from 3-d to 2-d growth occurs when the binding energy to the substrate exceeds the binding between two QLs ($\approx 0.14$ J/m$^2$) and is delineated by the shaded region in Fig. 5 (c). For 2-d growth, the height of the resulting nanoplate is a single QL and the overall shape of the nanoplate is determined from the corresponding 2-d Wulff construction- where the distances of the crystal edges from a point within the 2-d crystal plane are proportional to the corresponding edge energies which are approximated from the surface and binding energy[43]. This yields an nonequiside hexagon with lateral surfaces $(01\bar{1}5)$ and $(0\bar{1}15)$ as shown in inset (III) of Fig. 5 (c). Increasing the binding further yields continued reduction in $l_s$ and shrinks the area of the corresponding $(0\bar{1}15)$ surface until a secondary crit-

ical point in which $l_s=0$, occurring when the substrate binding becomes 0.28 J/m$^2$. For larger substrate binding, the $(0\bar{1}15)$ is no longer a terminal surface and the equilibrium shape maintains an equilateral triangle consisting of three lateral $(01\bar{1}5)$ surfaces as shown in the inset labeled (IV). We note that for the LDA calculations, the qualitative evolution of the energy minimizing shape is identical to what has been found for revPBE+LAP, the difference being the binding necessary to transition between 3-d and 2-d growth and the transition to an equilateral triangle occur at 0.32 and 0.46 J/m$^2$, respectively.

## IV. CONCLUSIONS

Using first-principles calculations, we have performed a detailed study of the stability of the non-basal surfaces of $Bi_2Te_3$. Quite insensitive to the level of theory, we establish the stability in order of increasing energy as $(0001)\rightarrow(01\bar{1}5)\rightarrow(11\bar{2}0)\rightarrow(01\bar{1}0)\rightarrow(01\bar{1}$ X$)\rightarrow(01\bar{1}4)$-A/B$\rightarrow(01\bar{1}\bar{1})$-A/B$\rightarrow(02\bar{2}\bar{5})$. This result was unchanged under the LDA and GGA functionals, with and without the inclusion of spin-orbit interaction or LAP corrections to account for the description of vdW interactions in the self-consistent calculations. Furthermore, we have shown that this energy ordering can be largely understood in the context of simple counting of the dangling bonds associated with each surface. Given the great stability of the $(01\bar{1}5)$ surfaces, they are expected to be quite prominent in as-grown samples leading to non-vertical termination at the edges. The Wulff construction of free-standing $Bi_2Te_3$, for example, is terminated by three $(01\bar{1}5)$ and three $(0\bar{1}15)$ surfaces forming a regular hexagon midplane. Binding to the substrate was found to greatly alter this equilibrium shape, leading to an irregular hexagon which transitions to a large flat triangle in the presence of increasing substrate binding. Understanding the energetics of the non-basal surfaces of $Bi_2Te_3$ not only provides insight into as-grown samples, but may also aid in the preparation of specific surfaces for topological applications.

[*] Electronic address: damienwest@gmail.com (D.W.)

[1] L. Fu and C. L. Kane, Phys. Rev. Lett. **102**, 216403 (2009).

[2] L. Fu and C. L. Kane, Phys. Rev. B **76**, 045302 (2007).

[3] X.-L. Qi, R. Li, J. Zang, and S.-C. Zhang, Science **323**,

1184 (2009).

[4] X.-L. Qi and S.-C. Zhang, Rev. Mod. Phys. **83**, 1057 (2011).

[5] M. Z. Hasan and C. L. Kane, Rev. Mod. Phys. **82**, 3045 (2010).

[6] M.-H. Xie, X. Guo, Z.-J. Xu, and W.-K. Ho, Chinese Physics B **22**, 068101 (2013).

[7] L. He, X. Kou, and K. L. Wang, physica status solidi (RRL) ÂšC Rapid Research Letters **7**, 50 (2013).

[8] X. Chen, X.-C. Ma, K. He, J.-F. Jia, and Q.-K. Xue, Advanced Materials **23**, 1162 (2011).

[9] D. Kong, W. Dang, J. J. Cha, H. Li, S. Meister, H. Peng, Z. Liu, and Y. Cui, Nano Letters **10**, 2245 (2010).

[10] Y. Yan, Z.-M. Liao, Y.-B. Zhou, H.-C. Wu, Y.-Q. Bie, J.-J. Chen, J. Meng, X.-S. Wu, and D.-P. Yu, Sci. Rep. **3** (2013).

[11] C.-Y. Moon, J. Han, H. Lee, and H. J. Choi, Phys. Rev. B **84**, 195425 (2011).

[12] L. Seixas, D. West, A. Fazzio, and S. B. Zhang, Nature Communications **6**, 7630(2015).

[13] O. Shunsuke and I. Nobuyuki, Jpn. J. Appl. Phys. **33**, L470 (1994).

[14] M. Li, J. B. Hannon, R. M. Tromp, J. Sun, J. Li, V. B. Shenoy, and E. Chason, Phys. Rev. B **88**, 041402 (2013).

[15] M. Safdar, Q. Wang, M. Mirza, Z. Wang, and J. He, Crystal Growth & Design **14**, 2502 (2014).

[16] C.-X. Liu, X.-L. Qi, H. Zhang, X. Dai, Z. Fang, and S.-C. Zhang, Phys. Rev. B **82**, 045122 (2010).

[17] Y. L. Chen, J. G. Analytis, J. H. Chu, Z. K. Liu, S. K. Mo, X. L. Qi, H. J. Zhang, D. H. Lu, X. Dai, Z. Fang, et al., Science **325**, 178 (2009).

[18] G. Kresse and J. Furthmüller, Comp. Mater. Sci. **6**, 15 (1996).

[19] P. E. Blöchl, Phys. Rev. B **50**, 17953 (1994).

[20] P. Jurecka, J. Sponer, J. Cerny, and P. Hobza, Phys. Chem. Chem. Phys. **8**, 1985 (2006).

[21] H. J. Monkhorst and J. D. Pack, Phys. Rev. B **13**, 5188 (1976).

[22] J. P. Perdew, K. Burke, and M. Ernzerhof, Phys. Rev. Lett. **77**, 3865 (1996).

[23] W. Kohn and L. J. Sham, Physical Review **140**, A1133 (1965).

[24] Y. Zhang and W. Yang, Phys. Rev. Lett. **80**, 890 (1998).

[25] Y. Y. Sun, Y.-H. Kim, K. Lee, and S. B. Zhang, The Journal of Chemical Physics **129**, 154102 (2008).

[26] W. Zhang, R. Yu, H.-J. Zhang, X. Dai, and Z. Fang, New Journal of Physics **12**, 065013 (2010).

[27] D. West, Y. Y. Sun, H. Wang, J. Bang, and S. B. Zhang, Phys. Rev. B **86**, 121201 (2012).

[28] W. Liu, X. Liu, W. T. Zheng, and Q. Jiang, Surf. Sci. **600**, 257 (2006).

[29] A.-C. Shi and M. Wortis, Phys. Rev. B **37**, 7793 (1988).

[30] V. L. Deringer and R. Dronskowski, Chemphyschem **14**, 3108 (2013).

[31] P. L. Gutshall and G. E. Gross, J. Appl. Phys. **36**, 2459 (1965).

[32] C. Franchini, V. Bayer, R. Podloucky, G. Parteder, S. Surnev, and F. P. Netzer, Phys. Rev. B **73**, 155402 (2006).

[33] R. Wahl, J. V. Lauritsen, F. Besenbacher, and G. Kresse, Phys. Rev. B **87**, 085313 (2013).

[34] B. Meyer, Phys. Rev. B **69**, 045416 (2004).

[35] K. Reuter and M. Scheffler, Phys. Rev. B **65**, 035406 (2001).

[36] J. Wang, J. Liu, Y. Xu, J. Wu, B.-L. Gu, and W. Duan, Phys. Rev. B **89**, 125308 (2014).

[37] R. W. G. Wyckoff, *Crystal Structures*, vol. 1 (Interscience Publishers, New York, 1963), 2nd ed.

[38] I. V. Markov, *FRONT MATTER* (WORLD SCIENTIFIC, NJ, USA, 2003), pp. i–xviii.

[39] W. Lu, Y. Ding, Y. Chen, Z. L. Wang, and J. Fang, J. Am. Chem. Soc. **127**, 10112 (2005).

[40] W. Wang, J. Goebl, L. He, S. Aloni, Y. Hu, L. Zhen, and Y. Yin, J. Am. Chem. Soc. **132**, 17316 (2010).

[41] M. Ferhat, J. C. Tedenac, and J. Nagao, J. Cryst. Growth **218**, 250 (2000).

[42] W. L. Winterbottom, Acta Metallurgica **15**, 303 (1967).

[43] V. I. Artyukhov, Y. Hao, R. S. Ruoff, and B. I. Yakobson, Physical Review Letters **114**, 115502 (2015).